Automated manufacturing process for sustainable prototyping of NMR transceivers

Sagar Wadhwa[2,3], Nan Wang[2], Klaus-Martin Reichert[1], Manuel Butzer[1], Omar Nassar[2], Mazin Jouda[2], Jan G. Korvink[2], Ulrich Gengenbach[1], Dario Mager[2], and Martin Ungerer[1]

[1]Institute for Automation and Applied Informatics (IAI), Karlsruhe Institute of Technology (KIT), Hermann-von-Helmholtz-Platz 1, 76344 Eggenstein-Leopoldshafen, Germany

[2]Institute of Microstructure Technology (IMT), Karlsruhe Institute of Technology (KIT), Hermann-von-Helmholtz-Platz 1, 76344 Eggenstein-Leopoldshafen, Germany

[3]Voxalytic GmbH, Rosengarten 3, 76228 Karlsruhe, Germany

Correspondence: Dario Mager (dario.mager@kit.edu)

Abstract

Additive manufacturing has enabled rapid prototyping of components with minimum investment in specific fabrication infrastructure. These tools allow a fast iteration from design to functional prototypes within days or even hours. Such prototyping technologies exist in many fields, from 3-dimensional mechanical components, or printed electric circuit boards (PCBs) for electrical connectivity, to mention two. In the case of nuclear magnetic resonance (NMR) spectroscopy one needs the combination of both fields, we need to fabricate three-dimensional electrically conductive tracks as coils that are wrapped around a sample container. Fabricating such structures is difficult (e.g. 6 axes micro-milling) or simply not possible with conventional methods. In this paper, we modified an additive manufacturing method that is based on the extrusion of conductive ink to fast-prototype solenoidal coil designs for NMR. These NMR coils, need to be as close to the sample as possible and by their shape have specific inductive values. The performance of the designs was first investigated using EM-field simulations, and circuit simulations. The coil found to have optimal parameters for NMR was fabricated by extrusion printing and its performance was tested in a $1.05\ \mathrm{T}$ imaging magnet. The objective is to demonstrate reproducible rapid prototyping of complicated designs with high precision that as a side effect hardly produces material waste during production.

1 Introduction

Additive manufacturing of electrical tracks with widths in the range of tens of microns both in 2D and 3D providing low electrical resistances is of great interest for electronics applications such as interconnects, wire-bonds, sensors, antennas, transistors, transparent electrode grids (Paulsen et al., 2012; Adams et al., 2011; Can et al., 2019; Jang et al., 2013; Ahn et al., 2009).

Low viscosity inks ($< 20\,\mathrm{mPas}$), as frequently used in ink-jet printing, are highly susceptible to surface forces, and therefore tend to develop irregular structural topographies, especially with respect to nonuniform distribution of the ink (Kwon et al., 2020). The aspect ratio of a printed line describes the quotient of layer thickness and width. This ratio should be as high as possible in order to achieve sufficient conductivity when miniaturizing the line width. Typical aspect ratios of single-layer (single pass) inkjet-printed conductor tracks, for example, are often less than 0.01 (Ungerer et al., 2017). High-viscosity inks (in general pastes) allow higher solid loading, which leads to lower resistances (20-70% of the bulk conductivity) and are also less prone to irregular topographies. These inks allow much higher aspect ratios, e.g. up to 0.14 for silver conductors on polyimide (Ungerer et al., 2024). In the class of digital printing processes, the extrusion printing (EP) process (contact dispensing) enables printing of inks with the highest viscosities (Kwon et al., 2020; Ungerer, 2020). Extrusion printing is based on the ink transfer from the printing nozzle (dispensing tip) to the substrate by means of a continuous fluidic bridge forming a fluid filament during relative motion between the nozzle and substrate (Ungerer et al., 2024). The force for generating the fluidic bridge and for maintaining the appropriate ink mass flow during printing is applied to the ink by means of dispensing principles e.g. time-pressure, positive displacement (piston) or rotary screw (Auger pump) (Kwon et al., 2020). Ungerer et al. (2024) developed a versatile and modular EP system based on the time-pressure principle and tested it for various screen printing inks and printing nozzle types. MD Ashif et al. (2024) applied this printing principle for the fabrication of radio frequency (RF) transmission lines for photonic integrated circuits. They pointed out the robustness of the process against substrate properties and the far better line edge quality on ceramic substrates in contrast to transmission lines inkjet printed with low viscosity inks. The extrusion printing technology and the modular system presented by Ungerer et al. (2024) show great potential to fabricate NMR coils, to directly print complicated coil geometries on a glass tube. This helps in improving the filling factor of the coil and allows the use of different sample geometries based on the requirements of the measurements.

NMR is one of the most specific spectroscopy techniques available, and is able to elucidate structures down to the atomic level. However, the acquisition of a well-resolved spectrum depends on several factors, such as the homogeneity of the static magnetic field, which needs to be in within parts per billion, achieved by the minimisation of the magnetic susceptibility mismatch caused by material jumps in the vicinity of the detector. The resonator coil must be properly tuned and matched, and sufficient SNR (signal-to-noise ratio) must be available. Field homogeneity corrections can be achieved with shimming coils, and typically depends strongly on the spectroscopist's experience. The simplest coil types are solenoids, but there are much more sophisticated coil designs that differ in signal quality and signal to noise ratio (SNR). If we look at the equation of the SNR by Hoult and Richards (1976),

$$SNR \propto \frac{k V_\mathrm{s} B_1}{\sqrt{R}}, \tag{1}$$

where, V_s is the volume of the sample, k is the filling factor of the coil, B_1 is the magnetic field produced by the coil, and R is the resistance of the coil. As the SNR of the coil also depends on the volume of the sample and the filling factor, therefore, a low volume results in a lower SNR value. However, this effect can be compensated by improving the filling factor of the coil, which helps to improve the SNR, especially of micro-coils, where not all parts can be shrunk equally. To get a decent

filling factor of the coil, the conductive part responsible for generating the radiofrequency (RF) magnetic field must be as close as possible to the sample Kamberger et al. (2016). However, the size of the coil and the length of the conductive track also affect the coil's self-resonance. If the self-resonance is below the nucleus's Larmor frequency it cannot be tuned and matched to that frequency using capacitors, and if the self-resonance is too high, the tuning and matching to the lower frequency are limited by the available capacitance values Hoult and Richards (1976). Hence, the coil needs to be designed such that it fulfils both the requirement of the filling factor and at the same time can be tuned and matched to the target frequencies. Coils are normally simulated before fabrication, but in the case of microcoils the conventional fabrication methods have significant tolerances, which lead to large variations from coil to coil. In this work, we present a routine which eliminates the need for repeated prototyping to get dedicated coil parameters. The coil design and fabrication cycle starts with the development of a three-dimensional solenoid geometry model, which is used to compute the RF magnetic field radiation, and the S-parameters (reflection and transmission coefficients) at the termination port of the coil using COMSOL AB. The S-parameters are used to calculate the coil's electrical properties such as self-resonance of the coil, lumped component values required for tuning and matching at the target frequency, and the quality factor at the target frequency using Advanced Design System (ADS) from Keysight Technologies. After investigating all the parameters, the coil, which best meets the requirement is manufactured using the extrusion printing technology. The performance of the coil was tested by acquiring NMR spectrum and MR images. The objective is to make the method easily scalable for industrial applications with a sustainable method, as it was shown by Moxley-Paquette et al. (2024), as developing suitable micro-coils can lead to several iterations before a functional design is found. The idea to make micro-MR coils Olson et al. (1995) in a non-manual way has been around for quite a while like in the following publications Rogers et al. (1997); Mager et al. (2009); Badilita et al. (2010a); Fischer et al. (2013). In this paper, we plot the full route from the planning of a coil with desired properties to its manufacturing and testing. But why bother in the first place about new fabrication technologies? Conventional solenoidal microcoils can simply be hand-wound Olson et al. (1995) and yield excellent results. One reason is that there are other coil designs than just solenoids, i.e. Helmholtz, birdcage, or saddle coils to mention a few Haase et al. (2000). These designs cannot be manufactured manually at the micro-scale. The second reason for direct coil writing is the improved precision. Every material change next to the sample causes disturbances in the magnetic field homogeneity, that is especially a problem for materials that need to be close to the sample like the micro-coil itself. Therefore, it is good to know these disturbances upfront so that they can be minimised by design, reducing the magnetic field disturbances that need to be corrected by pre-disturbing the field (so-called shimming). Also, the electrical tuning and matching gets easier if the coils show small part-to-part variations. The gain that comes from the high geometrical precision is a little bit reduced by the reduced conductivity of sintered metal tracks compared to bulk wires. The sintered tracks show around 20-70% of the bulk conductivity, leading to a slightly higher electrical noise.

2 From simulation-based design to specific coils

The closer the coil is to the sample, the better the filling factor and the subsequent improvement in SNR, as described in Eq. 1. The smaller size of the glass tube requires coils in the same dimensional range, which results in higher self-resonance.

Though higher self-resonance can be tuned and matched to lower target frequencies, the tuning range is limited by the available capacitance values. Another factor that plays an important role is that by shrinking the coil, the conductive tracks diameters are also reduced to be able to get well defined geometries, but these thinner tracks lead to higher resistance of the coil since the cross-sectional area of the conductor is lower Kamberger et al. (2016). The increase in resistance raises the thermal noise of the coil and reduces its RF efficiency ($B_1/\sqrt{W}$). However, to significantly increase the noise the temperature should dramatically increase. On the other hand, the lower the resistance the better the RF efficiency.

To find the perfect geometry, which meets all the requirements a computational domain was set up to simulate the coils' RF behaviour. For the computation, various solenoid geometries were investigated, where the diameter of the coils were kept constant at $1.5\,\mathrm{mm}$, and the number of turns N and the pitch p i.e., the distance between two turns were varied. For the simulation, the sample material chosen was H_2O, where the sample volume was approximated by a cylindrical geometry of height $1\,\mathrm{mm}$ and diameter $1\,\mathrm{mm}$. The glass tube was neglected in the simulation since it would increase the complexity of the calculation without having a major effect on the result, due to the low dielectric constant. The sample volume was kept constant for different coil geometries to simulate the uniform influence of the sample on the coil properties. The computation of the model was performed using the RF module from COMSOL AB. The computational geometries and the truncation of the boundaries are described in Fig. 1(a). Mathematically, the COMSOL model is summarised as:

$$\nabla \times (\nabla \times \boldsymbol{E}) - \omega_0^2(\epsilon_r\epsilon_0\mu_r\mu_0 - \iota\frac{\mu_r\mu_0\sigma}{\omega_0})\boldsymbol{E} = 0 \qquad \text{in } \Omega, \tag{2}$$

$$\boldsymbol{n} \times \boldsymbol{E} = 0 \qquad \text{on } \delta\Omega \tag{3}$$

$$\sqrt{\frac{\mu_0\mu_r}{\epsilon_0\epsilon_r - \iota\sigma/\omega}}\boldsymbol{n} \times \boldsymbol{H} + \boldsymbol{E} - (\boldsymbol{n}\cdot\boldsymbol{E})\boldsymbol{n} = -\boldsymbol{E_s} + (\boldsymbol{n}\cdot\boldsymbol{E_s})\boldsymbol{n} \qquad \text{on } \delta\Omega_{Coil} \tag{4}$$

where $\boldsymbol{E}$ is the RF electric field in $\mathrm{V\,m^{-1}}$, $\boldsymbol{E_s}$ is the RF electric field on the surface of the domain in $\mathrm{V\,m^{-1}}$, $\boldsymbol{H} = \boldsymbol{B}/(\mu_0\mu_r)$ is the RF magnetic field strength, ϵ_0 and ϵ_r are the free space and relative permittivity respectively, μ_0 and μ_r are the free space and relative permeability respectively, σ is the conductivity of the coil's material, $\boldsymbol{n}$ is the normal vector, and ω is the RF angular frequency. The computational domain was meshed using tetrahedral elements. The coil was truncated using the impedance boundary condition available in COMSOL, with this the coil's domain could be excluded from the computation. The frequency range for the calculation used was from $1\,\mathrm{GHz}$ to $3\,\mathrm{GHz}$, where the frequency was swept in the steps of $0.5\,\mathrm{GHz}$ using adaptive frequency sweep. The lumped port for RF excitation was connected between the coil's terminals port, where the port's resistance was set at $50\,\Omega$ to minimise insertion losses. The self-resonance of the coil was calculated using the reactance of the coil, where the frequency at which the reactance was zero was considered to be the self-resonance frequency. The RF-efficiency was calculated by the formula

$$\text{RF-efficiency} = \frac{B_1}{\sqrt{P}}, \tag{5}$$

Coil #	Turns #	Pitch [mm]	Self-resonance [GHz]	RF-efficiency [kHz/$\sqrt{\text{W}}$] ([µT/$\sqrt{\text{W}}$])
1	5	0.300	2.06	13.11 (307.9)
2	6	0.300	1.83	14.84 (348.5)
3	7	0.300	1.65	16.29 (382.53)
4	5	0.525	2.62	10.72 (251.91)
5	6	0.525	2.27	11.62 (273.05)
6	7	0.525	2.02	12.29 (288.62)
7	5	0.750	2.93	8.75 (205.44)
8	6	0.750	2.55	9.21 (216.38)
9	7	0.750	2.24	9.51 (222.34)

Table 1. Different coils simulated, their self-resonance and RF-efficiency calculated by the averaged B_1 field on the sample region for 1 W of power applied for ^{1}H at 45 MHz. A cylindrical sample geometry with a diameter of 1 mm, and height of 1 mm was taken as a standard for all the coil geometries.

where B_1 is the total induced magnetic field in the sample volume in [T], and P is the RF power applied in W. For the calculation, B_1 was calculated at 45 MHz, which is the Larmor frequency of ^{1}H in a magnetic field of 1.05 T. The results are summarised in Table 1.

The S-parameters generated from the electromagnetic simulation were exported as S1-Parameter files and used in the circuit simulation to determine the effective self-resonance and quality factor of the coil when mounted on a printed circuit board (PCB). For the circuit simulation, Advanced Design System 2015.01 from Keysight Technologies was used. The PCB on which the coil was to be mounted for the measurement on the Vector network analyser (VNA) was modelled as shown in Figure 2(a), where the effect of the PCB on the coil parameters was determined by measuring the impedance between the ports, with the port's impedance set to 50 Ω to minimise insertion losses. The influence of the conductive adhesive used to connect the printed coil to the PCB, is probably the biggest source of variance in the setup. However since it is an unknown variation it was neglected in the simulation, and an idealised value was used. Similar to the method above, the frequency where the reactance was zero is reported as the self-resonance of the coil. The quality factor Q of the coil was calculated at 45 MHz using the formula

$$Q = \frac{\omega L}{R} \tag{6}$$

where in the numerator, ωL is the reactance of the coil, such that ω is the angular frequency and L is the inductance, and in the denominator R is the resistance at 45 MHz. The result for various coil geometries is summarised in Table 2

From the simulation results, it was found that the coil with a pitch p of 0.525 mm and five turns, best fitted the requirements, since it could be tuned and matched with standard fixed-valued discrete capacitors as our intention was to avoid the use of bulky non-magnetic trimmer capacitors. Moreover, it had a decent quality factor and was sensitive enough to be used as a transceiver

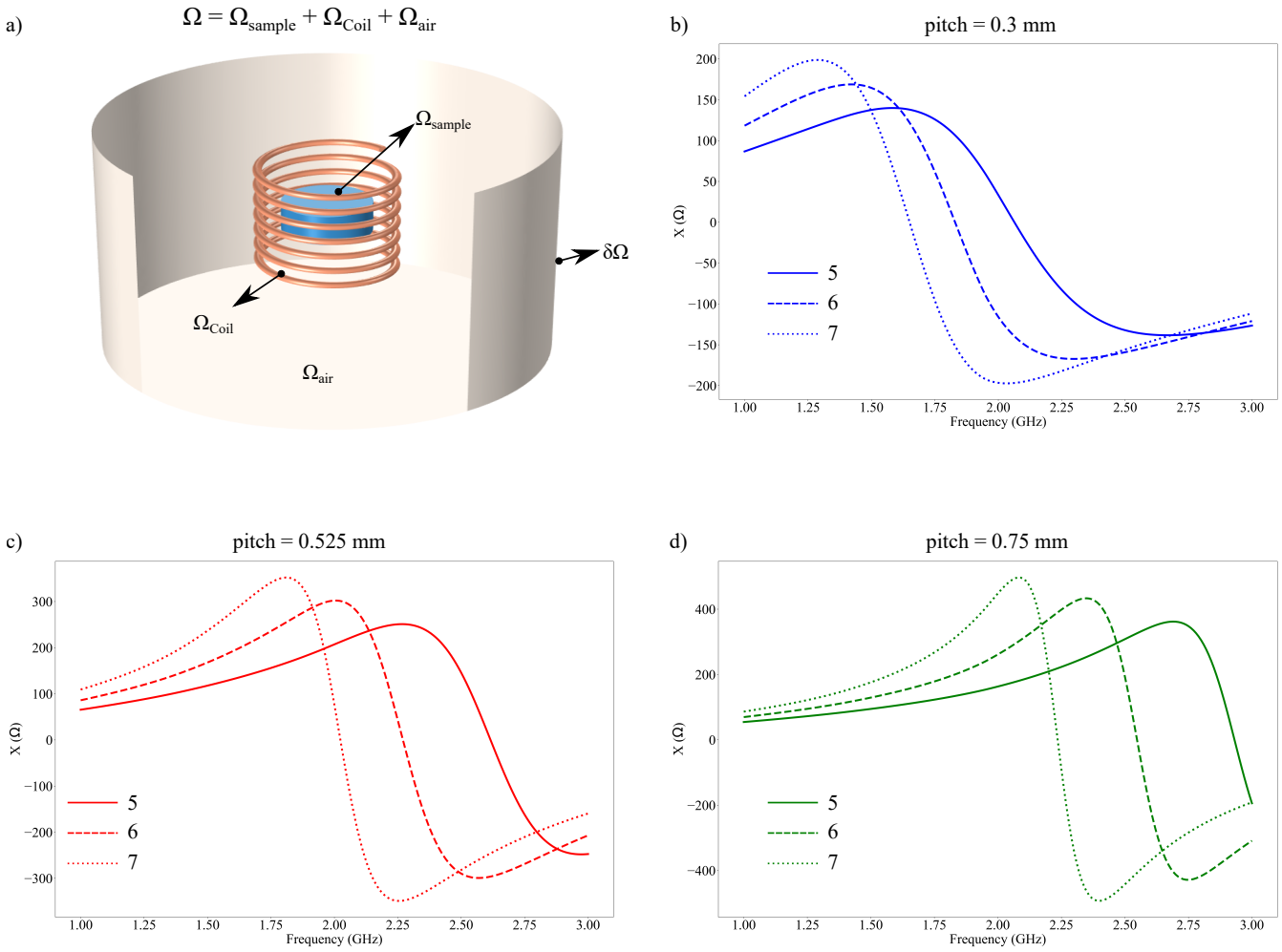

Figure 1. (a) Computational setup with different domains. The computational domain (Ω) was truncated by a perfect electric boundary condition. The lumped port was connected to the coil's terminal, where the S-parameters were calculated from 1 GHz to 3 GHz, and the magnetic field produced by the coil at 45 MHz, i.e., the Larmor frequency of ^{1}H at 1.05 T. (b)-(d) Reactance of the coil simulated from the S-parameters, with different pitch p and number of turns N. The frequency at which the reactance is zero is reported as the coil's self-resonance.

coil. The S1P files from the EM-field simulations and the circuit simulations for all the coils are available as the dataset with the article, which can be used to determine the coil's characteristics at different frequencies.

3 Fabrication of the coil

The challenging part of fabricating MR micro-coils is the choice and design of the support structures for the coils since the material properties affect the static magnetic field Finch et al. (2016). Different materials such as polymide, Wang et al. (2017),

Coil #	Q-factor [.]	Self-resonance (with PCB) [MHz] ([MHz])	Self-resonance (w/o PCB) [GHz]	Inductance nH(nH)	Resistance Ω(Ω)
1	2.907(3.156)	685 (540)	2.06	287.2(49.18)	27.93(4.42)
2	2.614(4.035)	548 (520)	1.83	388.7(56.57)	42.04(3.98)
3	2.306(4.172)	434 (480)	1.65	507.9(64.24)	62.27(4.37)
4	6.828((2.874)	839 (670)	2.63	216.7(42.28)	8.97(4.17)
5	6.729(3.295)	724 (630)	2.27	282.7(47.26)	11.88(4.07)
6	6.424(3.443)	620 (600)	2.02	357.4(52.31)	15.73(4.31)
7	10.924(2.788)	910 (680)	2.93	181.0(39.13)	4.68(3.98)
8	11.277(3.152)	817 (660)	2.55	229.7(42.71)	5.76(3.84)
9	11.130(3.353)	727 (640)	2.24	282.9(39.70)	7.19(3.97)

Table 2. The Q-factor, self resonance,inductance, and resistance of the electrical circuit, the latter data comparing simulation and measurement results (in brackets). The coil is placed directly on the PCB shown in the figure 2(a). The self-resonances without the PCB are the simulation results from table 1.

SU-8, Spengler et al. (2016), Teflon, Finch et al. (2016) etc. have been used as support structures. Existing techniques for fabricating micro-coils for NMR are using photolithographic methods, wire-bonding, rolling up of 2-D printed structures, or by milling (Spengler et al., 2016; Badilita et al., 2010b; Kratt et al., 2009; Wang et al., 2018, 2017; Nassar et al., 2021; Moxley-Paquette et al., 2024; Chia Gómez et al., 2013). Out of this list MEMS-like fabrication processes would be favourable due to their well established high precision and repeatability. However, designing a coil directly on a cylindrical glass sample container (or on 3D structures) is complicated since available MEMS processes focus on planar substrates. Nevertheless, to fabricate 3D or complex structured coils, a fabrication technique based on extrusion printing can allow to achieve the requirements (Ungerer et al., 2024). Extrusion printing allows to extrude highly viscous, metal-nanoparticle inks, e.g. commercially available conductive screen printing inks, through customized glass printing nozzles for direct deposition on planar substrates and 3D parts such as glass capillaries (Ungerer et al., 2024). Hence, we combine the advantages of commercial screen printing inks with those of digital printing processes to reproducibly fabricate microcoils directly on glass tubes.

The extrusion printing system applied consists of a granite table (A) carrying two linear stages arranged crosswise on top of each other to form a xy-stage as shown in Figure 3. A gantry (B) is mounted on the table, which carries an additional linear stage as the z-axis of the cartesian motion system. The printhead (C) is mounted on the carriage of the z-axis. For printing onto cylindrical substrates such as glass tubes, we developed an adapted, motorized dividing head that is mounted onto the xy-stage. The dividing head consists of a goniometer stage (D) as well as a rotary stage (E) for manual alignment of the tube axis parallel to the y-axis. Onto this setup the rotational axis (B) composed of a mechanical support, a stepper motor with a flexible shaft coupling (F) for turning the substrate and a bearing block with clamps (G) to mount cylindrical substrates are fixed. Furthermore, the EP system comprises two optical systems (H and I).

The optical system (H) consists of a USB 3.0 camera and a Navitar microscopic lens. Together with a LED for transmitted light illumination it is applied for manual alignment of the tube in parallel to the y-axis as well as for control of the distance

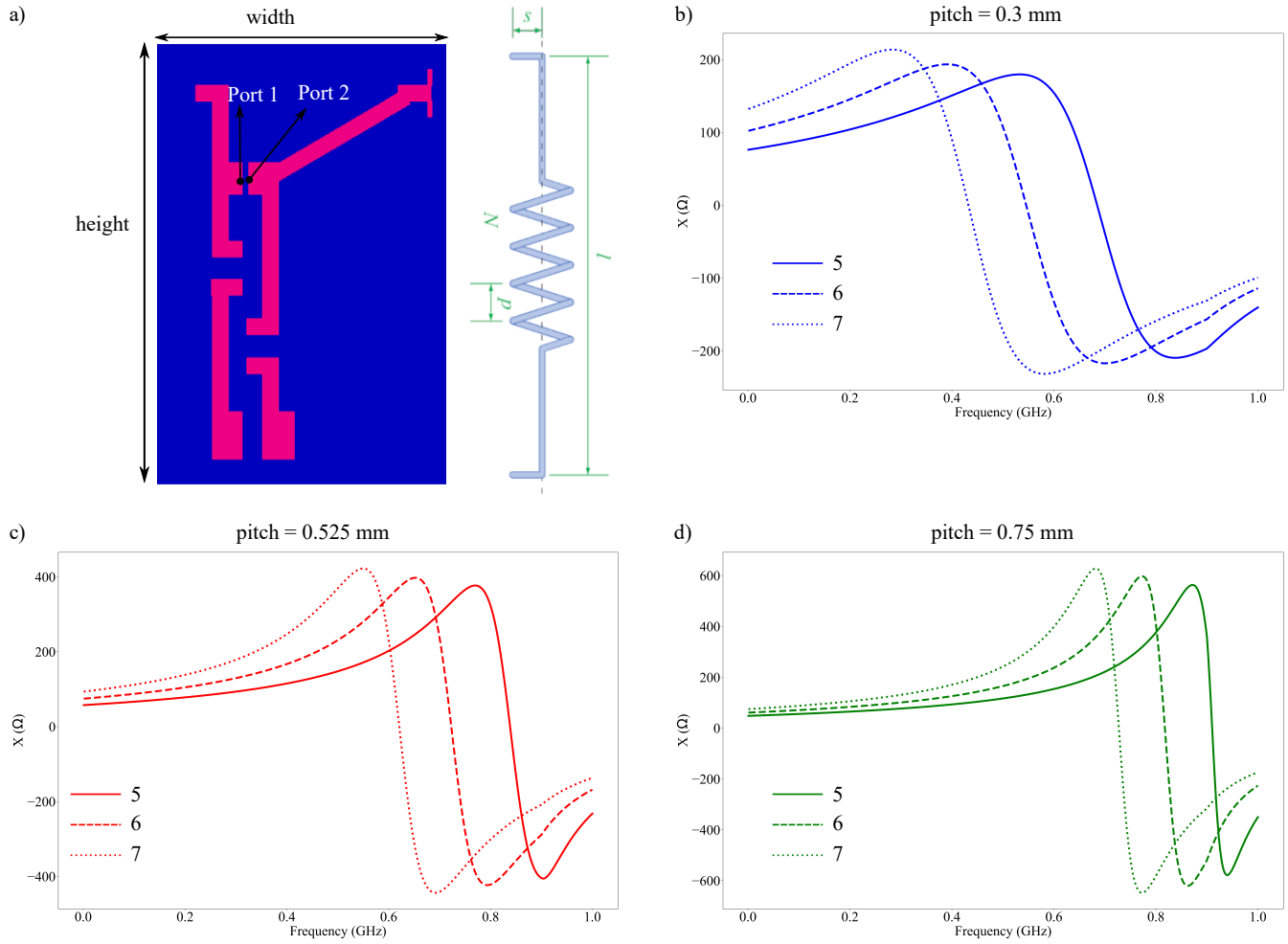

Figure 2. (a) The PCB used for the simulation, where the geometry was determined from the PCB which was used for the measurement from the VNA. The height of the PCB was 49 mm, and the width was 15 mm. Next to it is a schematic of a solenoidal coil. (b)-(d) Reactance of the coil mounted on the PCB shown in (a), with different pitch p and number of turns N. The frequency at which the reactance is zero is reported as the setup's self-resonance.

between nozzle and substrate. The second optical system (I) composed of a GigE camera and a borescope with coaxial incident light illumination is used for manual aligment of the substrate relatively to the printhead.

160 The printhead is composed of a $3\,\mathrm{cm}^3$ syringe barrel that is fixed on the z-axis via a magnetic clamping setup, a printing nozzle and a syringe barrel adapter that connects the cartridge to a time-pressure dispensing unit. As control system the Beckhoff basic CPU module CX1020-0123 with software PLC TC1260 TwinCAT 2 is used in combination with stepper motor terminals and digital input/output terminals. After manual setting of the local coordinate system of the PCB by means of a Logitech F310 Joystick the printing process runs automated, controlled by the TwinCAT software.

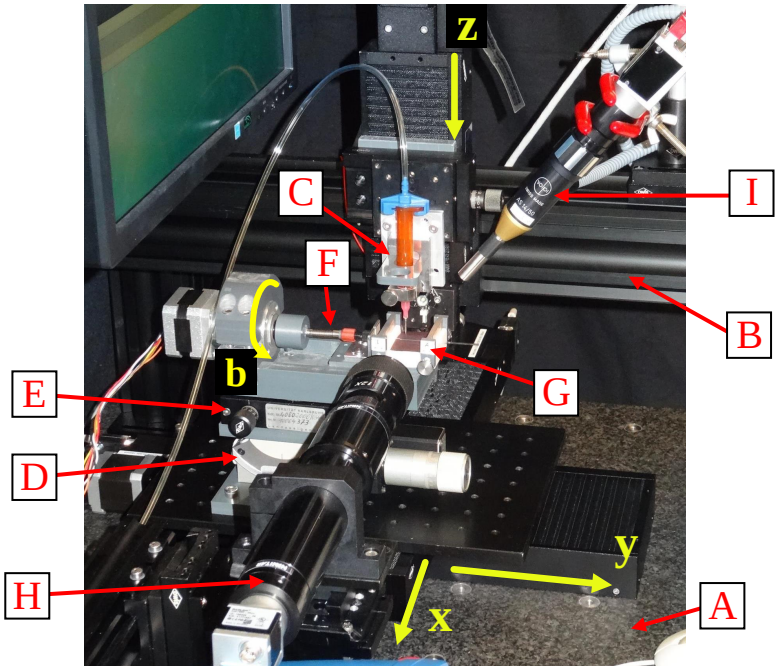

Figure 3. Extrusion printing system for cylindrical substrates. Main components are granite table (A), gantry (B), printhead (C), xybz-stage, goniometer stage (D) with rotary stage (E), flexible shaft coupling (F), bearing block (G), optical systems (H) and (I).

The NMR microcoils are printed onto borosilicate glass tubes with a length of $101.6\,\mathrm{mm}$, an inner diameter of $1.0\,\mathrm{mm}$ and an outer diameter of $1.5\,\mathrm{mm}$ (World Precision Instruments (WPI): PG52151-4). As conductive ink, the thixotropic screen printing paste NPS from Harima filled with silver nanoparticles (nominal size $12\,\mathrm{nm}$) was selected. According to the certificate of analysis, the batch applied has a metal content of $82.3\,\mathrm{wt\text{-}\%}$. A shear thinning behaviour was confirmed by means of plate/plate rheometry measurements: about $510\,\mathrm{Pa\,s}$ at a shear rate of $5\,\mathrm{s}^{-1}$ and $44\,\mathrm{Pa\,s}$ at $50.2\,\mathrm{s}^{-1}$ (Ungerer et al., 2024).

The coil type to be realized was the solenoid coil as depicted in Figure 2 (a), where the parameters, a constant pitch p, and the number of turns N, were chosen from the geometry simulated as shown in Table 1. The overall length l and the length s of the contact line end was based on the connection point on the PCB (as shown in Figure 2 (a)) where the coil was to be mounted. Each coil variation presented in Table 1 was printed three times, in order to assess the reproducibility of the fabrication process in terms of the electrical properties of the coils.

As discovered in first printing tests, the glass tubes onto which the coils were to be printed, showed variances in geometric tolerances such as total runout, straightness and cylindricity. These variances resulted in varying distance between the nozzle and the cylindrical surface of the tube during printing. Neglecting the tolerances, reproducible printing without distance control between nozzle and tube is not possible. As there will always be fabrication tolerances from the tube manufacturing process, this issue was solved by the means of optical inspection and sorting of the tubes prior to printing. Glass tubes with an overall radial deviation of more than $8\,\mu\mathrm{m}$ were rejected. Thus, a package of 100 tubes WPI PG52151-4 led to a rejection rate of about $22\,\%$.

Following the methodology described by Ungerer et al. (2024), a glass capillary with $d_i = 50.6\,\mu\mathrm{m}$ as printing nozzle was used for printing with a pressure p in the range of $2.85\,\mathrm{bar}$ to $2.98\,\mathrm{bar}$ (without backpressure p_{vac}), a distance $\Delta z = 35\,\mu\mathrm{m}$ between nozzle and substrate and a printing speed of $v_p = 15\,\mathrm{mm\,min^{-1}}$.

After printing the silver inks are dried, cured and sintered in a Memmert UP 500 oven for $60\,\mathrm{min}$ at $220\,^\circ\mathrm{C}$ and then stored at room temperature. Silver-filled, expoxy based conductive adhesive Henkel Loctite 3880 is used for mounting the manufactured coils onto PCBs for electrical analysis and NMR measurements. Prior to mounting, the silver solenoid coils are surface treated for $60\,\mathrm{s}$ at $0.44\,\mathrm{mbar}$ and $15\,\mathrm{W}$ in a low-pressure Argon-plasma (Diener Atto plasmacleaner with $13.56\,\mathrm{MHz}$) to remove silver oxides. The glass tubes with the solenoid coils are cut to length to match the width of the PCB. To mount the coils to the PCB's contact pads, the tubes are manually aligned under a stereoscopic microscope. Conductive adhesive (Loctite 3880) is manually applied onto the PCB contact pads by use of a gauge 20 dispensing tip and a time-pressure dispenser. The resulting bonds are cured in an oven for $15\,\mathrm{min}$ at $130\,^\circ\mathrm{C}$. The assembly was then visually inspected for printing defects through macroscopic images. Figure 4 gives an overview of the printed and mounted coil variants. For each variant, one of three realized coils is shown.

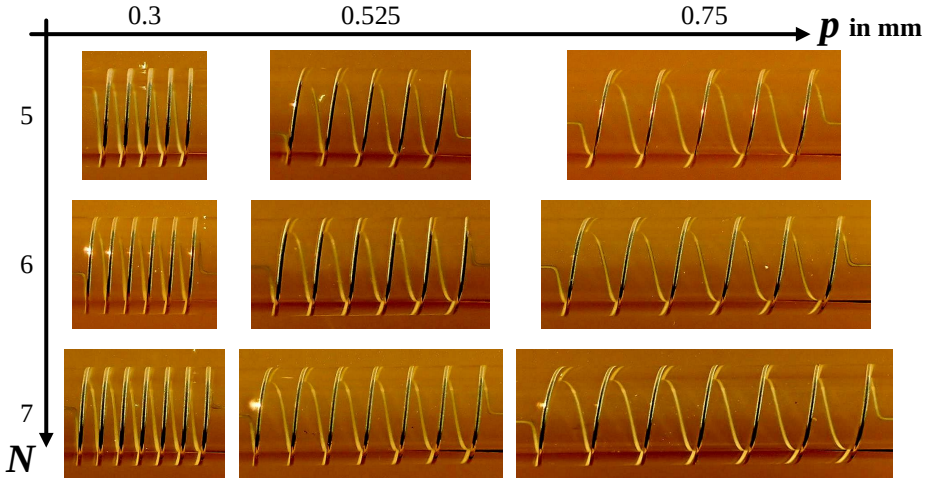

Figure 4. Extrusion printed solenoid coil variants on glass tubes.

In addition to the visual inspection, the turns of a few coils are analysed in terms of width, thickness and cross section by means of a Keyence VK-9700 confocal laser scanning microscope (LSM). Figure 5 shows the assembly of a coil with $p = 0.3\,\mathrm{mm}$, $N = 5$ on a PCB (A), a microscopic image of one of the adhesive joints (B) made of conductive adhesive between the PCB and the printed contact line. Furthermore, a microscopic image (C) and its LSM height profile (D) of a winding section is depicted. For this coil the LSM-measurements yield a structure width of $59.2\,\mu\mathrm{m}$, a thickness of $8.34\,\mu\mathrm{m}$ resulting in an aspect ratio of 0.14 and a cross section of $317\,\mu\mathrm{m}^2$. The aspect ratio of a printed line describes the quotient of layer thickness and width. This ratio should be as high as possible in order to achieve sufficient conductivity when miniaturizing the line width.

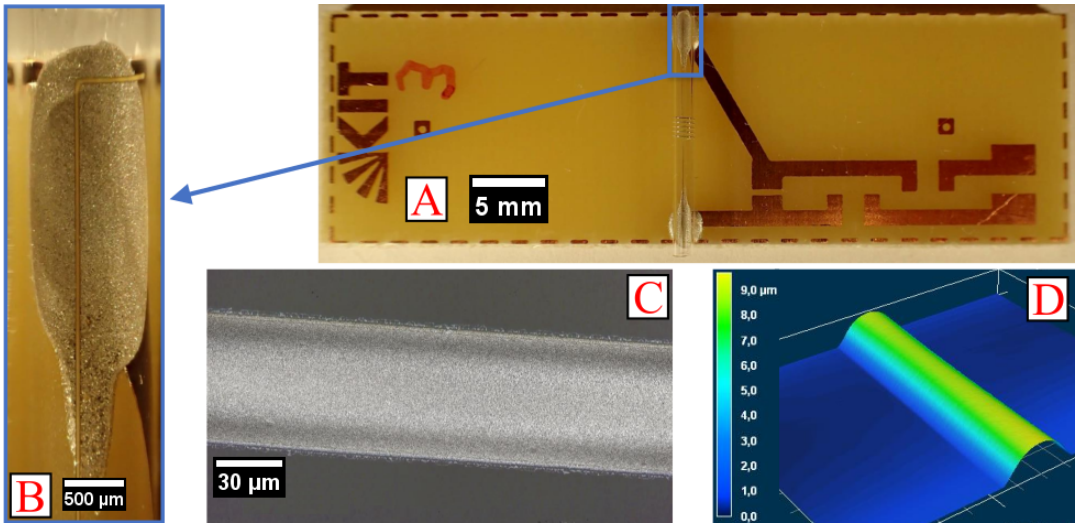

Figure 5. A solenoid coil with the parameters p = 0.3 mm and $N = 5$ mounted on a PCB (A) with detail of the contact (B). Microscopic image (C) and LSM height profile (D) of a winding section.

Using an impedance analyzer Agilent E4991A and a probe station Cascade Microtech MPS150 all the realised NMR-coil-PCB assemblies are analysed in terms of the parameters resistance R, inductance L, modulus of the impedance $|Z|$ and quality factor Q over a measuring frequency in the range of 1 MHz to 2000 MHz with 801 points. The resistance values were measured at the frequency of 4.98 MHz, which was an arbitrarily chosen value as it was far away from the ^{1}H frequency used in the measurement, and the resistance values were similar to the DC resistance.

Both impedance analysis and LSM inspection show the high reproducibility of the realized coils and assemblies. Figure 6 substantiates this statement showing the reactance of various samples of two coil parameter sets. The progression of the measurement curves for all three coils of a parameter set is almost identical. These properties are the same for the measured resistance and modulus of impedance as well.

This reproducibility is only true for the extrusion printed coil structures. Conductive adhesive (Loctite 3880) is used to connect the copper tracks to the PCB. To estimate the impedance of these adhesive contacts three PCBs on which no coils but rods of copper wire (diameter 1.08 mm) are mounted were measured. At 4.98 MHz the resistance has a mean of 0.0701 Ω and a standard deviation of 0.0398 Ω. The high standard deviation reflects the poor reproducibility of manual adhesive dispensing and coil mounting. Nevertheless these results show that the resistance of the conductive adhesive joints can be neglected for the realized coils. Based on microscopic measurements and calculations, the total conductive length of some solenoid coils between both adhesive joints is determined. In combination with the LSM profile measurements the resistivity of one of three coils with $N = 5$ and $p = 0.3$ mm is calculated as 3.96 µΩ cm. This value is obtained from the coil's serial resistance of 4.17 Ω at 4.98 MHz minus the mean value of the copper rod assembly and corresponds to about 2.5 times of the resistivity of bulk silver at 298 K (David R. Lide, ed., 2005).

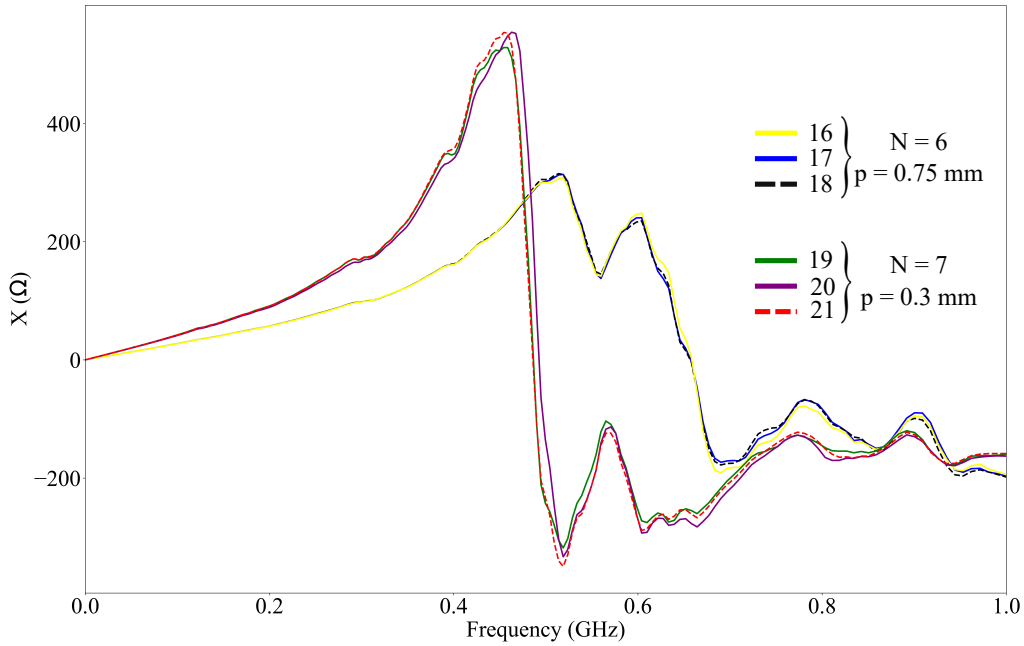

Figure 6. Coils' reactance X over frequency f of three solenoid coils with $N = 6$ and $p = 0.75\,\mathrm{mm}$ and of three coils with $N = 7$ and $p = 0.3\,\mathrm{mm}$.

4 Proton magnetic resonance spectrosocopy and imaging at 1.05 T

The NMR spectrum and images were acquired in a horizontal bore $1.05\,\mathrm{T}$ imaging magnet, (ICON, Bruker). The coil had a pitch p of $0.525\,\mathrm{mm}$ with 5 turns. The combined coil and capillary was mounted on the PCB as shown in Figure 7(a). The PCB was slightly different from the one used for simulating the S-parameters, due to the magnetic field direction and restricted space inside the magnet. Nevertheless, the coil was also tuned to $45\,\mathrm{MHz}$ and matched to $50\,\Omega$.

For acquiring the NMR spectrum, the glass capillary supporting the extrusion printed coil was filled with pure ethanol. The excitation power applied to the coil was $0.1\,\mathrm{W}$, with a $\pi/2$ pulse duration of $27\,\mu\mathrm{s}$, and a receiver gain of 203. The spectrum was acquired with a single scan. It is plotted in Figure 7(b), using the Python library "nmrglue" (Release 0.9-dev, Date December 05, 2021). From the spectrum, the RF efficiency measured was $29.28\,\mathrm{kHz}/\sqrt{\mathrm{W}}$, the SNR of the triplet at around $1.3\,\mathrm{ppm}$ was 538.65.

The MR images acquired are shown in the Figure 7(c)-(f). In the respective order the images acquired were (c) a sagittal image and (d) an axial image of a capillary completely filled with distilled water. Similarly, (e) shows a sagittal image and (f) an axial image of a capillary filled with distilled water around an unfilled Teflon tube with an outer diameter of $0.5\,\mathrm{mm}$. While (c) and (d) show the signal to noise of the coil, the Teflon tube in (e) and (f) was used to provide a recognizable structure that can highlight the achievable spatial resolution.

For image acquisition, the pulse sequence used was a gradient-echo sequence with an echo time (TE) of 4 ms, a repetition time (TR) of 100 ms, flip angle (FA) of 30°, slice thickness of 2 mm, image size of 128 px × 128 px, and a 10 mm × 10 mm field of view (FOV) resulting in an in-plane resolution of 78 µm. The number of scans was 32 for sagittal images and 64 for axial images. The signal-to-noise ratio (SNR) values of the MR images are 68, 36, 58, and 17 respectively.

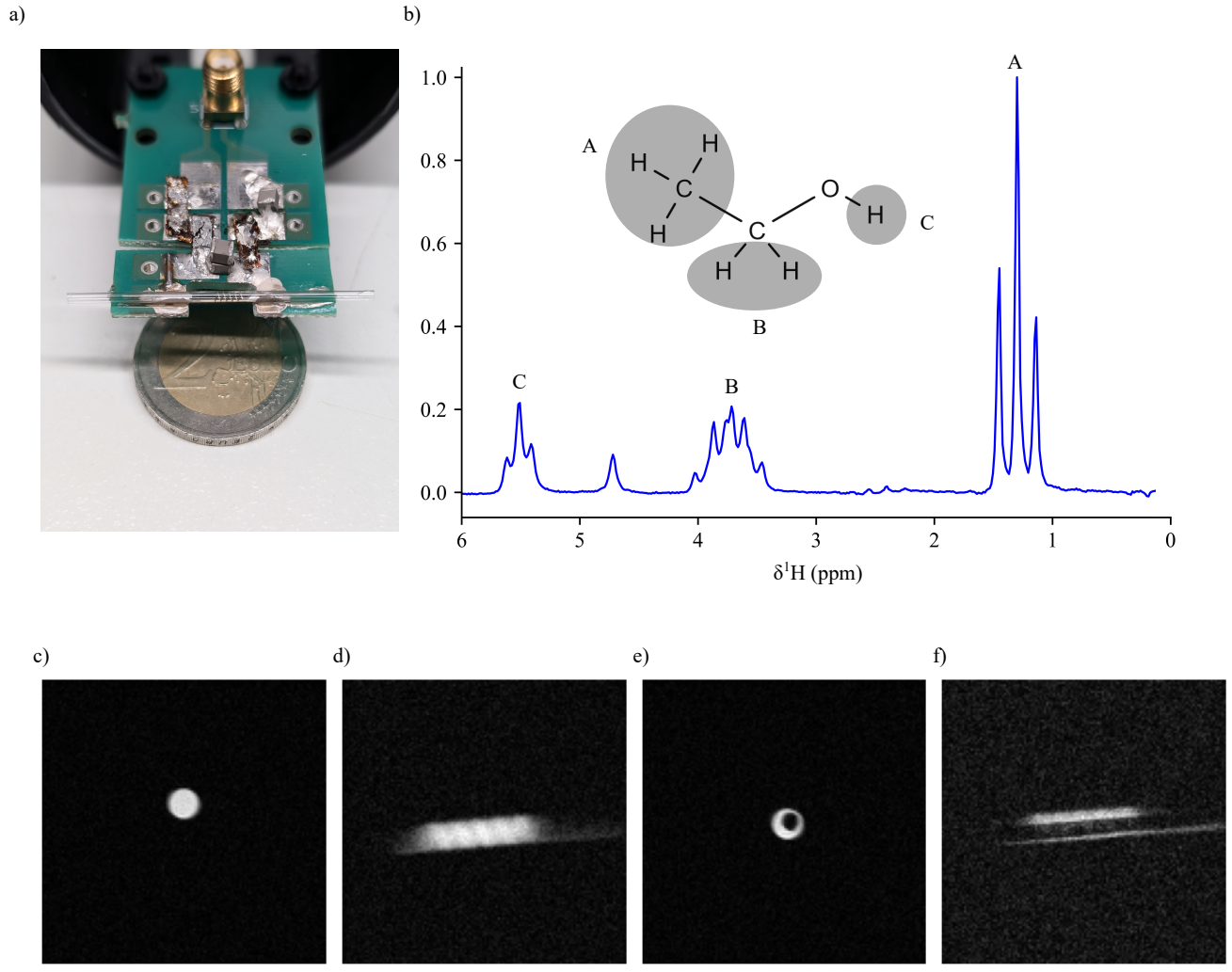

Figure 7. (a) The glass capillary with the printed coil used for the acquisition with the sample inside. (b) Homonuclear ^{1}H NMR spectrum of pure ethanol acquired in a 1.05 T imaging magnet (RF excitation power of 0.1 W, $\pi/2-$pulse duration of 27 µs). (c-f) MR images with the coil, figure (c) and (d) with a completely filled capillary show a sagittal and an axial image respectively. Figure (e) and (f) also shows a sagittal and an axial image but with a 0.5 mm-outer-diameter Teflon tube placed in the capillary and the sample filled around it. Since Teflon (C_2F_4) has no ^{1}H nuclei, it has no ^{1}H NMR signal. This creates a defined border and highlights the spatial resolution achievable.

5 Conclusion

In this article, we demonstrated a method for rapidly prototyping coils using modeling, simulation and additive manufacturing. The geometry of the coils was computed for their efficiency, i.e., the magnetic fields generated for the power applied to the coils, and their self-resonance. From these computations, the reflection parameters were generated, which were used in the simulation of the printed circuit boards on which the coil were to be mounted. This helped to provide the effective self-resonance of the system, which was significantly lowered than the actual computed values. Therefore, the coil which had a decent quality factor, RF-efficiency, and could be tuned to the Larmor frequency of ^{1}H, was chosen for the fabrication.

The coils were additively manufactured by extrusion printing on glass capillaries and tested in a $1.05\,\mathrm{T}$ horizontal bore imaging magnet. The spectrum of pure ethanol was recorded, where the coil could distinguish J-coupling even in low field values. The splitting shown in the spectrum due to J-coupling shows the spectral quality of the coils. Similarly, the MRI results demonstrate the high sensitivity of the printed coil enabling high-resolution imaging with decent SNR.

These results show the NMR compatibility of the coils, which can now be rapidly produced with a low iteration process tailored to the application of both spectroscopy and imaging. Solenoids were chosen in this study because this type allows to clearly demonstrate the effects of design parameter variation and repeatability.

In future studies, we also want to apply this modelling, simulation, extrusion printing workflow to investigate other more general coil classes like birdcage or butterfly coil that are otherwise very complicated to fabricate.

The limitations of the extrusion printing process in terms of resolution and minimisation of the line width are mainly determined by the properties of the ink in terms of particle size and rheology, especially regarding its thixotropic behaviour. The linewidth can be be reduced by reducing the nozzle orifice. This also affects the distance between the nozzle and the substrate during printing. This distance can be approximated to be 0.5x the inner diameter of the nozzle orifice. For very small nozzle orifice, precise automatic control of the distance between the nozzle and substrate is the key. Measuring sub-micron deviations in the stand-off distance when rotating the glass tubes, to be printed on, is challenging and had its limitations with the measurement equipment available when the device was built. Printing linewidths in the range of hundreds of microns was possible but reducing the linewidth further would have led to a reduced conductor's cross-section and hence decreasing the conductivity of the printed tracks. In addition, the tracks need to withstand a certain current. This also limits the miniaturisation of the printed conductor. The pitch of the coils can be reduced to the point where the windings tend to touch when the pitch is equal to the linewidth. For even smaller pitches, a multilayer printing approach is required with additional isolating layers. Vice versa the linewidth can be increased at a constant pitch until the tracks tend to touch. The line thickness strongly depends on the rheology of the ink. Printing parameters and the surface of the glass only have minor influences on the thickness. To increase the thickness of the tracks, the rheology must be adjusted towards higher viscosity and a certain thixotropic of the behaviour inks. For higher aspect ratios, multi-pass printing instead of single-pass can be a solution, but this can affect the track's edge quality. The main issue when changing the outer diameter of the coil is an appropriate mounting of the tube with the changed diameter. Larger variations in tube diameter due to tube fabrication tolerances probably require a revision of the setup for

mounting the tubes. Certainly, a diameter of 150 µm will be challenging and probably not compatible with the bearing blocks of the presented system but feasible with a modification of the setup.

A future improvement of the extrusion printing equipment lies in the implementation of a closed-loop control of the distance between the printing nozzle and the sample container. This would reduce the requirements on low dimensional tolerances of commercial glass tubes and would thereby further simplify the process. Moreover we intend to improve mounting of the printed coils onto the PCBs and also include it in the modelling and simulation to even more precisely forecast printed coil performance. The flexibility of the printing system allows for complicated shapes and precision which can now be directly fabricated on the sample container. The coils produced with our method show so small sample-to-sample variation that the tuning and matching of the samples becomes very easy and could for example be done with a low-cost tuning and matching circuit Jouda et al. (2020).

Acknowledgements

The authors would like to thank T. Scharnweber at KIT-IBG 1 for providing access to a laser scanning microscope, and B. Hochstein at KIT-MVM for the rheometric analysis of the Harima NPS ink. Furthermore, the authors would like to thank J. Martel for fabricating the glass printing nozzle. SW acknowledges Helmholtz Research Area Information, in its program Materials Systems Engineering, for a (VirtMat) scholarship. MJ acknowledges the partial funding from the DFG projects SFB 1527/1 – project-ID 454252029 (HyPERiON) and CRC 1537 (ECOSENSE). NW, DM, and JK acknowledge support of the German Research Foundation, (DFG-RUMS) project KO-1883-23-1.

Contributions

The authors contributed in the following fields: Idea of the paper: NW, JGK, UG, DM, MU Planing of experiments: All LabWork: SW, NW, ON, KMR, MB, MU Simulations: SW, NW, ON, MJ Interpretation of results: SW, NW, MJ, DM UG, JGK, MU Writing of Manuscript: SW, ON, MJ, UG, JGK, DM, MU

Conflict of interests

J.G.K. is is a member of the editorial board of Magnetic Resonance and a shareholder in Voxalytic GmbH, a company that produces NMR equipment. S.W. is an employee at Voxalytic GmbH. The other authors declare no conflict of interest.

References

Adams, J. J., Duoss, E. B., Malkowski, T. F., Motala, M. J., Ahn, B. Y., Nuzzo, R. G., Bernhard, J. T., and Lewis, J. A.: Conformal Printing of Electrically Small Antennas on Three-Dimensional Surfaces, Advanced Materials, 23, 1335–1340, https://doi.org/10.1002/adma.201003734, 2011.

Ahn, B. Y., Duoss, E. B., Motala, M. J., Guo, X., Park, S.-I., Xiong, Y., Yoon, J., Nuzzo, R. G., Rogers, J. A., and Lewis, J. A.: Omnidirectional Printing of Flexible, Stretchable, and Spanning Silver Microelectrodes, Science, 323, 1590–1593, https://doi.org/10.1126/science.1168375, 2009.

Badilita, V., Kratt, K., Baxan, N., Mohmmadzadeh, M., Burger, T., Weber, H., Elverfeldt, D. v., Hennig, J., Korvink, J. G., and Wallrabe, U.: On-chip three dimensional microcoils for MRI at the microscale, Lab Chip, 10, 1387–1390, https://doi.org/10.1039/C000840K, 2010a.

Badilita, V., Kratt, K., Baxan, N., Mohmmadzadeh, M., Burger, T., Weber, H., Elverfeldt, D. V., Hennig, J., Korvink, J. G., and Wallrabe, U.: On-chip three dimensional microcoils for MRI at the microscale, Lab on a chip, 10, 1387–1390, https://doi.org/10.1039/c000840k, 2010b.

Can, T. T. T., Nguyen, T. C., and Choi, W.-S.: Patterning of High-Viscosity Silver Paste by an Electrohydrodynamic-Jet Printer for Use in TFT Applications, Scientific Reports, 9, 1–8, https://doi.org/10.1038/s41598-019-45504-5, 2019.

Chia Gómez, L. P., Bollgruen, P., Egunov, A. I., Mager, D., Malloggi, F., Korvink, J. G., and Luchnikov, V. A.: Vapour processed self-rolled poly(dimethylsiloxane) microcapillaries form microfluidic devices with engineered inner surface, Lab Chip, 13, 3827–3831, https://doi.org/10.1039/C3LC50542A, 2013.

COMSOL: RF Module User's Guide, COMSOL Multiphysics v. 5.4, COMSOL AB, https://doc.comsol.com/5.4/doc/com.comsol.help.rf/RFModuleUsersGuide.pdf.

David R. Lide, ed.: Electrical Resistivity of Pure Metals, in: CRC Handbook of Chemistry and Physics, Internet Version 2005, edited by Lide, D. R., CRC Press, Boca Raton, FL, 2005.

Finch, G., Yilmaz, A., and Utz, M.: An optimised detector for in-situ high-resolution NMR in microfluidic devices, Journal of Magnetic Resonance, 262, 73–80, https://doi.org/https://doi.org/10.1016/j.jmr.2015.11.011, 2016.

Fischer, A. C., Korvink, J. G., Roxhed, N., Stemme, G., Wallrabe, U., and Niklaus, F.: Unconventional applications of wire bonding create opportunities for microsystem integration, Journal of Micromechanics and Microengineering, 23, 083 001, https://doi.org/10.1088/0960-1317/23/8/083001, 2013.

Haase, A., Odoj, F., Kienlin, M. V., Warnking, J., Fidler, F., Weisser, A., Nittka, M., Rommel, E., Lanz, T., Kalusche, B., and Griswold, M.: NMR Probeheads for In Vivo Applications, Concepts in Magnetic Resonance, pp. 388–388, https://doi.org/10.1002/1099-0534(2000)12:6, 2000.

Hoult, D. and Richards, R.: The signal-to-noise ratio of the nuclear magnetic resonance experiment, Journal of Magnetic Resonance, 24, 71–85, https://doi.org/https://doi.org/10.1016/j.jmr.2011.09.018, magnetic Moments, 1976.

Jang, Y., Kim, J., and Byun, D.: Invisible metal-grid transparent electrode prepared by electrohydrodynamic (EHD) jet printing, Journal of Physics D: Applied Physics, 46, 1–5, https://doi.org/10.1088/0022-3727/46/15/155103, 2013.

Jouda, M., Torres Delgado, S. M., Jouzdani, M. A., Mager, D., and Korvink, J. G.: ArduiTaM: accurate and inexpensive NMR auto tune and match system, Magnetic Resonance, 1, 105–113, https://doi.org/10.5194/mr-1-105-2020, 2020.

Kamberger, R., Moazenzadeh, A., Korvink, J. G., and Gruschke, O. G.: Hollow microcoils made possible with external support structures manufactured with a two-solvent process, Journal of Micromechanics and Microengineering, 26, 065 002, https://doi.org/10.1088/0960-1317/26/6/065002, 2016.

Kratt, K., Badilita, V., Burger, T., Korvink, J. G., and Wallrabe, U.: A fully MEMS-compatible process for 3D high aspect ratio micro coils obtained with an automatic wire bonder, Journal of Micromechanics and Microengineering, 20, 015 021, https://doi.org/10.1088/0960-1317/20/1/015021, 2009.

Kwon, K.-S., Rahman, M. K., Phung, T. H., Hoath, S., Jeong, S., and Kim, J. S.: Review of digital printing technologies for electronic materials, Flexible and Printed Electronics, 5, 1–53, https://doi.org/10.1088/2058-8585/abc8ca, 2020.

Mager, D., Badilita, V., Loeffelman, U., Smith, P. J., and Korvink, J. G.: Micro-MR coil construction by combining metal-on-glass inkjetting and MEMS techniques, in: Proceedings of the 17th Annual Meeting of ISMRM, 2009.

MD Ashif, N. R., Gengenbach, U., and Sieber, I.: Process Development for Digital Fabrication of Radio Frequency Transmission Lines with Off-the-Shelf Equipment, in: 2024 Symposium on Design, Test, Integration and Packaging of MEMS/MOEMS (DTIP), pp. 1–5, IEEE, https://doi.org/10.1109/DTIP62575.2024.10613213, 2024.

Moxley-Paquette, V., Pellizzari, J., Lane, D., Steiner, K., Costa, P. M., Wolff, W. W., Lysak, D. H., Ghosh Biswas, R., Downey, K., Ronda, K., Soong, R., Zverev, D., De Castro, P., Frei, T., Al Adwan-Stojilkovic, D., Graf, S., Gloor, S., Schmidig, D., Kuemmerle, R., Kuehn, T., Busse, F., Haberer, N., Domaszewicz, J., Scatena, R., Lacerda, A., Nashman, B., Anders, J., Utz, M., and Simpson, A. J.: Exploration of Materials for Three-Dimensional NMR Microcoil Production via CNC Micromilling and Laser Etching, Analytical Chemistry, 96, 13 588–13 597, https://doi.org/10.1021/acs.analchem.4c02373, pMID: 39116295, 2024.

Nassar, O., Jouda, M., Rapp, M., Mager, D., Korvink, J. G., and MacKinnon, N.: Integrated impedance sensing of liquid sample plug flow enables automated high throughput NMR spectroscopy, Microsystems & Nanoengineering, 7, 1–17, https://doi.org/10.1038/s41378-021-00253-2, 2021.

Olson, D. L., Peck, T. L., Webb, A. G., Magin, R. L., and Sweedler, J. V.: High-Resolution Microcoil 1H-NMR for Mass-Limited, Nanoliter-Volume Samples, Science, 270, 1967–1970, https://doi.org/10.1126/SCIENCE.270.5244.1967, 1995.

Paulsen, J. A., Renn, M., Christenson, K., and Plourde, R.: Printing conformal electronics on 3D structures with Aerosol Jet technology, in: 2012 Future of Instrumentation International Workshop (FIIW 2012), pp. 1–4, IEEE, Piscataway, NJ, https://doi.org/10.1109/FIIW.2012.6378343, 2012.

Rogers, J. A., Jackman, R. J., Whitesides, G. M., Olson, D. L., and Sweedler, J. V.: Using Microcontact Printing to Fabricate Microcoils on Capillaries for High Resolution Proton Nuclear Magnetic Resonance on Nanoliter Volumes, Applied Physics Letters, 70, 2464–2466, 570, 1997.

Spengler, N., Höfflin, J., Moazenzadeh, A., Mager, D., MacKinnon, N., Badilita, V., Wallrabe, U., and Korvink, J. G.: Heteronuclear Micro-Helmholtz Coil Facilitates micrometer-Range Spatial and Sub-Hz Spectral Resolution NMR of nL-Volume Samples on Customisable Microfluidic Chips, PloS one, 11, e0146 384, https://doi.org/10.1371/journal.pone.0146384, 2016.

Ungerer, M.: Neue Methodik zur Optimierung von Druckverfahren für die Herstellung funktionaler Mikrostrukturen und hybrider elektronischer Schaltungen, Dissertation, Karlsruher Institut für Technologie, Karlsruhe, 2020.

Ungerer, M., Spomer, W., Wacker, I., Schröder, R., and Gengenbach, U.: A Method for the Analysis of the Nano- and Micromorphology of Printed Structures on Flexible Polymer Films: Analysis of the cross section of inkjet-printed conductive traces on PET film substrates based on ultramicrotome sectioning and SEM imaging, International Journal on Advances in Intelligent Systems, 10, 383–392, 2017.

Ungerer, M. et al.: A reproducible extrusion printing process with highly viscous nanoparticle inks, Engineering Research Express, 6, Art. no. 015042, 2024.

Wang, N., Egunov, A., Spengler, N., Nestle, N., Luchnikov, V., Mager, D., and Korvink, J. G.: Inkjet Printed Micro Saddle Coil for MR Imaging, in: Proc. 32nd International Conference on Digital Printing Technologies (NIP), edited by Society for Imaging Science and Technology, vol. 2016, pp. 339–342, Springfield, VA, USA, 2017.

Wang, N., Meissner, M. V., MacKinnon, N., Luchnikov, V., Mager, D., and Korvink, J. G.: Fast prototyping of microtubes with embedded sensing elements made possible with an inkjet printing and rolling process, Journal of Micromechanics and Microengineering, 28, 1–10, https://doi.org/10.1088/1361-6439/aa7a61, 2018.